Strain localization and delamination mechanism of cold-drawn pearlitic steel wires during torsion

Aurélie Jamoneau, Denis Solas, Julie Bourgon, Pierre Morisot, Jean-Hubert Schmitt

To cite this version:

Aurélie Jamoneau, Denis Solas, Julie Bourgon, Pierre Morisot, Jean-Hubert Schmitt. Strain localization and delamination mechanism of cold-drawn pearlitic steel wires during torsion. Materials Science and Engineering: A, 2021, 814, pp.141222. ⟨10.1016/j.msea.2021.141222⟩. ⟨hal-03248400⟩

HAL Id: hal-03248400

https://centralesupelec.hal.science/hal-03248400v1

Submitted on 24 Apr 2023

HAL is a multi-disciplinary open access archive for the deposit and dissemination of scientific research documents, whether they are published or not. The documents may come from teaching and research institutions in France or abroad, or from public or private research centers.

L'archive ouverte pluridisciplinaire **HAL**, est destinée au dépôt et à la diffusion de documents scientifiques de niveau recherche, publiés ou non, émanant des établissements d'enseignement et de recherche français ou étrangers, des laboratoires publics ou privés.

Distributed under a Creative Commons CC BY-NC 4.0 - Attribution - Non-commercial use - International License

Version of Record: https://www.sciencedirect.com/science/article/pii/S0921509321004913
Manuscript_c8f107b63f3a6cae4c30a327900a8b4d

Strain localization and delamination mechanism of cold-drawn pearlitic steel wires during torsion

Aurélie JAMONEAU[1], Denis SOLAS[2], Julie BOURGON[3], Pierre MORISOT[1], Jean-Hubert SCHMITT[4*]

[1] Michelin, Centre de Technologies, 63000 Clermont-Ferrand, France
[2] Université Paris-Saclay, CNRS, ICMMO, 91405 Orsay, France
[3] Institut de Chimie et des Matériaux Paris-Est (ICMPE) UMR 7182 CNRS – Université Paris-Est, 2 Rue Henri Dunant, 94320 Thiais, France
[4] Université Paris-Saclay, CentraleSupélec, CNRS, Laboratoire de Mécanique des Sols, Structures et Matériaux, 91190, Gif-sur-Yvette, France

aurelie.jamoneau@michelin.com; denis.solas@universite-paris-saclay.fr; bourgon@icmpe.cnrs.fr; pierre.morisot@michelin.com; jean-hubert.schmitt@centralesupelec.fr

Abstract

Pearlitic steel wires are cold-drawn in order to attain high strength from the alignment of the pearlite colonies along the wire axis, as well as achieve a considerable reduction in the thickness of the ferrite lamellae. However, this high level of stress, in addition to surface defects and residual stresses, drastically decreases the strain ductility in tension and often in torsion. A significant limitation in torsion is the nucleation and growth of delamination cracks which propagate along the wire. Although this fracture phenomenon has long been studied, its origin and the underlying mechanisms remain debatable. This paper presents new microstructure investigations of drawn wires during torsion. The stages of initiation and propagation are defined towards a chronology of the development phases of delamination cracks based on the study of the microstructure of cold-drawn pearlitic steel wires before and after torsion. The curling of the grains leads to the creation of long grooves on the surface of the wire. These grooves increase stress concentration during twisting, thus localizing the formation of shear bands. Deformation and strain rate are so high in these bands that nanograins (10 to 30 nm) are formed. The delamination then appears to be mainly due to the localization of the single-shear deformation along the wire axis with mainly intergranular crack propagation.

Keywords

Precession assisted crystal orientation mapping technique; Pearlitic steel; Nanograins; Torsion loading; Delamination behavior; Shear band.

---

[*] Corresponding author: jean-hubert.schmitt@centralesupelec.fr

© 2021 published by Elsevier. This manuscript is made available under the CC BY NC user license
https://creativecommons.org/licenses/by-nc/4.0/

1. Introduction

Pearlitic steel is commonly used to process strong wires for cables. Wire rod is cold-drawn, which hardens the final wire up to 7 GPa for the highest-drawing reductions [1-4]. The resulting mechanical strength makes pearlitic wires essential components for structural engineering applications such as suspension bridge cables, tire cords, and springs. With a near eutectoid composition, pearlite is a composite of parallel ferrite and cementite lamellae, organized in colonies defined by a single ferrite crystallographic orientation and one orientation of the cementite lamellae [5-9].

During cold-drawing, pearlite colonies deform with most lamellae parallel to the direction in which the wire is drawn [10-14]. The deformation of ferrite results in a noticeable texture evolution, by which <110> axes progressively rotate toward the wire axis [15-19]. This evolution mostly leads to a <110> fiber texture while, for specific process parameters (some association of die angles and drawing reductions, for example), a <110> cyclic texture is reported for a fraction of the wire radius [15,20-22]. An axisymmetric drawing strain was deemed to require too large a plastic work in <110> grains. Thus, an intragranular plane strain, combined with a supplementary bending of the grain, is preferred to accommodate the macroscopic strain tensor [23]. This mechanism leads to grain curling in the wire cross-section, giving rise to an intricate microstructure sometimes called “Van Gogh’s skies” [21,24]. For large drawing reduction, cementite partly dissolves, and ferrite is oversaturated in carbon in solid solution [25-28]. Dissolution starts in ‘badly’ oriented pearlite colonies, for which the initial orientation of the cementite lamellae is nearly perpendicular to the wire rod [13,29]. At a very large strain, dynamic recovery of ferrite and cementite dissolution favor the decomposition of the pearlite microstructure in refined ferrite grains with high carbon content. Carbon is mainly segregated at the grain boundaries [30,31].

Beyond these microstructural evolutions, drawing generates high residual stresses and long grooves on the wire surface along the drawing direction [32-34]. During subsequent tension of a drawn wire, the combination of heterogeneous internal stresses along the wire radius, elongated pearlite microstructure, decrease of the interlamellar spacing, and carbon oversaturation of ferrite, all induce high yield stress and a smooth and long elasto-plastic transition [35-38]. As the work-hardening is very low due to the large plastic strain undergone by the wire, the high tensile stress dramatically reduces the total elongation in tension. It is no more than 2 to 3% for 3.5 drawing strain [35-40]. However, the fracture surface is still characteristic of a ductile fracture with a dimpled facies [36,41].

The torsion behavior is much better than tension, with large strain before fracture. This ductility allows for cabling drawn wires [40,42-44]. The rupture is ductile with a flat fracture surface for moderate drawing ratios and medium carbon content (close to eutectoid point) [42-45]. However, under some circumstances, a delamination crack initiates along the wire during torsion and propagates along the wire axis leading to a helical fracture surface [32,42,43,45-48]. Though many works have been dedicated to this problem, the origin and propagation mechanisms of delamination are yet to be fully understood. Some authors assume that delamination cracks initiate at small holes on the wire surface coming from the intersection of shear bands [32,42]. It is also reported that cracks originate at internal delamination under the wire surface [44]. The propagation mechanism is also under debate. A common approach is to evaluate the local stresses, including residual hoop stress, in the fracture mechanics frame [32,42,48,49]. Although, this can be criticized for very thin wires (diameter equal to or less than a few hundreds of micrometers). The fact that the surface of delamination cracks is relatively smooth with large flat plateaus and the rapid crack propagation along the wire axis led to the assumption that the rupture is mostly by cleavage [48]. This assumption could be reinforced by observing the fracture surface of a CT sample taken from an HPT deformed pearlite [48]: The fracture surface follows the highly deformed pearlite microstructure. This could also explain the negative influence of a circular texture, which gives rise to a majority of {111} cleavage planes parallel to the radial longitudinal planes of the wire [15]. However, other experimental facts contradict this mechanism. For instance, a recent study proves that delamination cracks are associated with a thin layer of fine grains [50]. Comparison with large shear strain under high-pressure torsion leads to the conclusion that it results from severe local plastic deformation. It is assumed that the fine-grained regions developed first during the torsion test. Then, delamination crack propagates through these regions, though this has not been proved directly.

This paper aims to understand further the initiation and propagation of delamination cracks during the torsion of a cold-drawn pearlitic wire. For comparison, two wires are studied: one giving rise to a regular behavior in torsion, the other displaying a delamination fracture. The microstructure is analyzed after cold-drawing, then local observations of the intragranular structure are performed during torsion, close to the wire surface and near stable and unstable cracks. FIB techniques in SEM allowed preparing thin foils, which are characterized by TEM and automated crystallographic orientation mapping coupling with precession (PACOM). After a description of the experimental procedures and the presentation of the main results, a discussion presents new hypotheses for delamination crack initiation and propagation mechanisms.

2. Experimental Procedure

Pearlitic steel wires (chemical composition in Table 1) were cold-drawn from a 1.73 mm diameter to 0.30 mm, up to a true strain of 3.5. The wires were coated with a thin layer of brass to improve lubrication during drawing. Two drawing schedules were imposed: the section reduction was the same at each drawing pass for both. It corresponded to a true strain between 0.13 and 0.17, accounting for the actual dispersion of an industrial process. For samples labeled ‘ND-samples’, the last step with a 0.02 true strain was added to the regular schedule. This is well-known for reducing the level of the residual stresses in longitudinal and hoop directions [51]. The other samples, without the final low reduction pass, are labeled ‘D-samples’.

***Table 1**: Chemical composition of the pearlitic steel wires*

	C	Mn	Si	Cr	Fe
wt.%	0.9	0.33	0.22	0.23	Bal.

Torsion tests were performed on a specific laboratory machine equipped with a torque sensor. Its capacity was up to 0.225 $kg.m^2.s^{-2}$ with an accuracy of 5.10^{-4} $kg.m^2.s^{-2}$. The shear strain γ is calculated from the twist angle θ and the wire length L:

$$\gamma = \frac{\theta r}{L} \qquad (1)$$

where r is the wire radius.

The current shear stress τ at a radius r is deduced from the measured torque T [52]:

$$\tau = \frac{1}{2\pi r^3}\left(3T + \theta \frac{dT}{d\theta}\right) \quad (2)$$

The torsion rate $\dot{\gamma}$ is estimated to be 0.6 s^{-1}.

SEM observations were performed either with a LEO GEMINI 1530 or with a FEI Helios 660, both equipped with an EBSD system from EDAX. The orientation imaging analysis was performed with TSL OIM Analysis. For EBSD analyses, transverse and longitudinal sections of wires were mechanically polished, then with a JEOL Cross Section Polisher. EBSD acquisitions were performed at a tension of 15 kV and an intensity of 0.8 nA. The step size was set between 10 and 20 nm.

FEI Helios ion beam enabled the TEM sample preparations. For observations close to a crack tip, the samples were prepared following the process previously described [53]: The crack tip was protected with a Pt layer, then a slice containing the crack was removed from the bulk and thinned.

Crystallographic orientation mappings were obtained using the precession assisted crystal orientation mapping technique. Maps and bright-field images were acquired on TEM samples with a Tecnai F20 using a NanoMEGAS ASTAR system [54]. The acquisition step was between 3 and 6 nm with a spot size of 7, which corresponds to a beam size of 3 to 4 nm.

3. Results

3.1. Microstructure of cold-drawn wires

As commonly reported, a large drawing reduction aligns the pearlitic colonies along the wire axis. A complex microstructure with curled grains develops in the cross-section. The local disorientation, the large density of dislocations, and the high level of internal stresses complicate an EBSD analysis: many pixels cannot be accurately indexed. However, the microstructure within a longitudinal section of the drawn wire is regular enough to be analyzed with conventional EBSD techniques [14,55,56]. The IPF map along the wire axis (z-axis) highlights that a large majority of grains have a <110> direction parallel to the axial axis, and few grains belong to the <112>//z component (Figure 1.a). At a drawing strain of 3.5, the grain diameter lies between 200 and 500 nm in the radial direction, their length being a few micrometers.

Statistical information is obtained if the EBSD map is large enough or several maps are averaged along the wire axis. This allows for pole figures to be calculated. {001} and {011} pole figures reveal a strong <110> texture (Figure 1.c). It cannot be deduced from these results if this is a fiber or a cyclic texture. However, since the measurements are made in the center of the wire, a <110> fiber texture may be assumed [55,57].

In the cross-section, the microstructure is wavy and intricate at large drawing strains. The local crystallographic orientation (Figure 2) is measured by scanning nanobeam and collected on Precession electron diffraction (PED) patterns. A cross-correlation comparison is made with simulated diffraction (ASTAR). Though the investigated area is much smaller than EBSD maps, the ribbon-like curled structure is evidenced: In the center of Figure 2.b, the S-shape grain (noted 'S'), with <101> parallel to the wire axis, is a typical example. The cementite lamellae are then bent to parallel the grain boundary as already observed [58] (Figure 2.a). The ribbons formed in the cross-section by these grains have an average length between 0.5 and 1 µm and a width between 50 and 150 nm. If the crystallographic orientation along the wire axis is quite constant within these grains, it seems that a {112} plane lies parallel to the longest boundary (Figure 2.c). This leads to a 30° disorientation along the S-grain length.

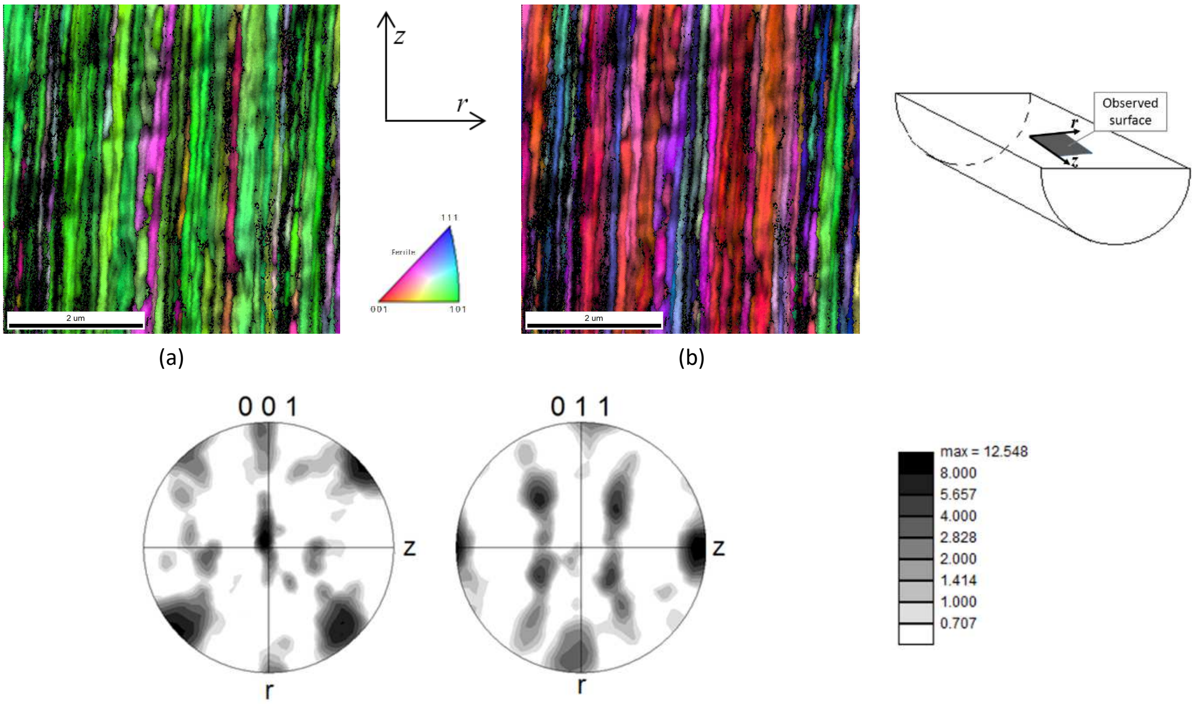

(a)

(b)

(c)

***Figure 1**: EBSD maps of grain orientations on a transverse plane: IPF in the longitudinal z (a) and radial r (b) directions, superimposed with image quality (GB = 15°)*
(c) {001} and {011} pole figures calculated from the EBSD data
(ND-sample; $\varepsilon = 3.5$).

Few grains, as the one noted 'A' in Figure 2.b, get away from the main <110> texture and are less likely to curve. However, their shape is far from equiaxed. It probably results from the constraints imposed by their neighboring <110> grains. Nevertheless, the orientation is rather homogeneous within the entire grain.

In some locations, large-angle disorientation is measured between neighboring elongated grains. Few nanograins, 30 to 100 nm in size, sometimes decorates the grain boundaries (see, for instance, area 'B' in Figure 2.c) and delineates a kind of 'kink band' crossing through the microstructure. A premise of such a microstructure can be evidenced in Langford's early work (see, for instance, Figure 4.E in [10]) though it is mostly subgrains rather than grain, probably due to a smaller drawing strain.

Since curling affects the entire cross-section, it must lead to irregularities at the surface. Depending on the grain curvature, curling creates protrusions and intrusions (Figure 3). Since grains are largely elongated along the wire axis, they are probably related to the longitudinal grooves observed on the wire surface after drawing. The microstructure has distinct similarities to cross-section observations along the wire central axis below the wire surface. However, under a sharp groove, grain curling is so localized and intense in <110> grain that a kink develops along the radial direction with several nanograins or subgrains (see area 'A' in Figure 3). The disorientation between from either side of the kink is about 60°. It probably comes from a groove, resulting from surface grain curling, which closed under the local compressive hoop stress at the wire surface during a next drawing pass [33].

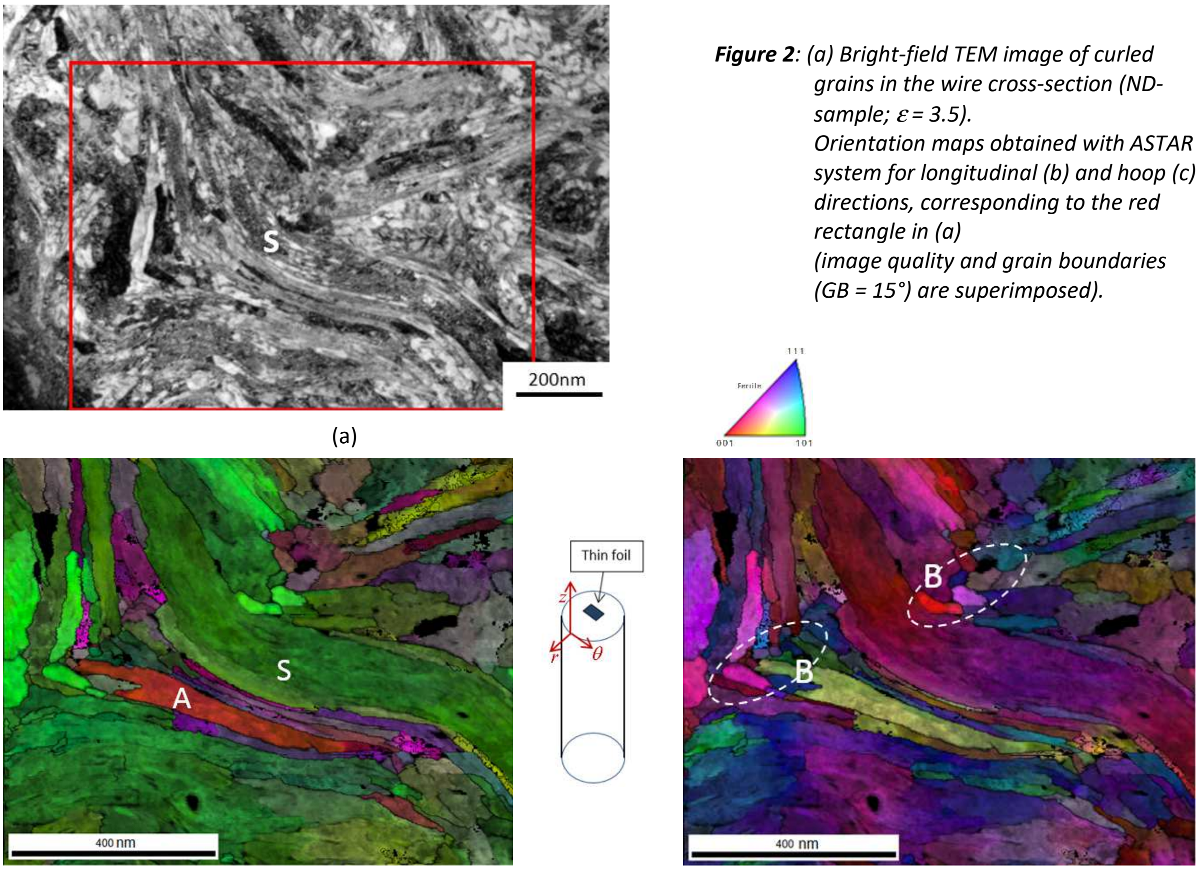

Figure 2: *(a) Bright-field TEM image of curled grains in the wire cross-section (ND-sample; $\varepsilon = 3.5$).*
Orientation maps obtained with ASTAR system for longitudinal (b) and hoop (c) directions, corresponding to the red rectangle in (a)
(image quality and grain boundaries (GB = 15°) are superimposed).

(a)

(b) (c)

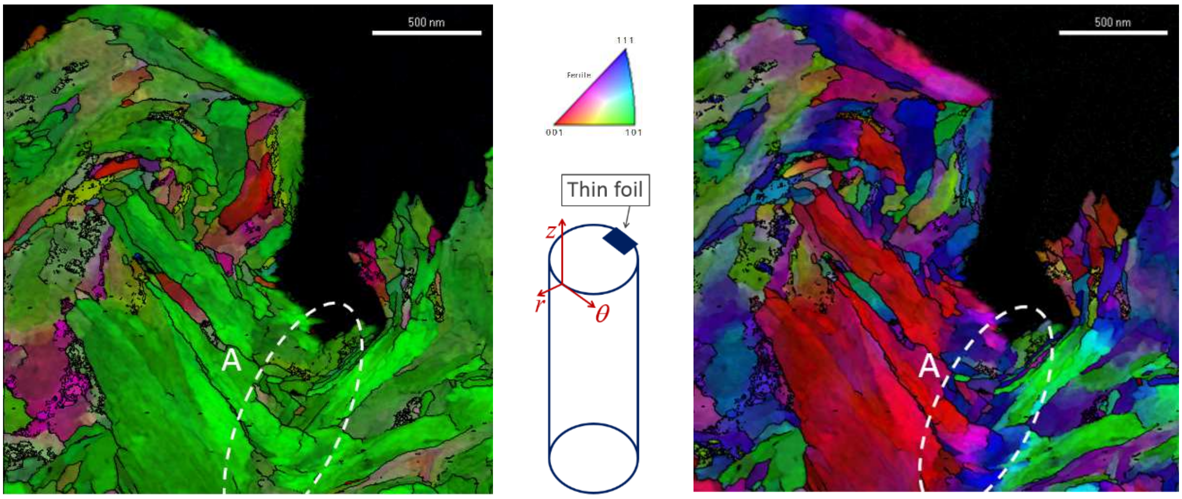

(a) (b)

Figure 3: *ASTAR orientation maps in the cross-section at the wire surface of ND-sample ($\varepsilon = 3.5$): in the longitudinal (a) and radial (b) directions (image quality and grain boundaries (GB = 15°) are superimposed).*

3.2. Torsion behavior

3.2.1. Mechanical behavior

After cold-drawing up to 3.5, ND- and D-samples were both deformed in torsion. Even after a large amount of cold-drawing, pearlitic wires still have a good ability to be twisted before fracture. The torque – strain curve for ND-sample is a perfect illustration of this behavior (Figure 4). The torsion's initial behavior is nearly the same for both samples: same shear modulus and yield stress. The influence of residual stresses, which results from the last pass, does not seem to affect the elastoplastic domain.

For D-sample, which did not experience the last pass with a low reduction, the torque drops sharply after the macroscopic yield stress. The behavior is typical of the delamination occurrence [40,42,44]: The sudden torque decrease corresponds to the crack propagation through the entire wire cross-section. The long plateau at a rather constant torque is associated with the delamination crack propagation along the wire axis. Finally, the torque increase after the plateau comes from the twist of the two-half wires and, in this way, is no longer representative of the actual behavior. The important consequence to remember is that the torque drop denotes the irreversible damage of the wire.

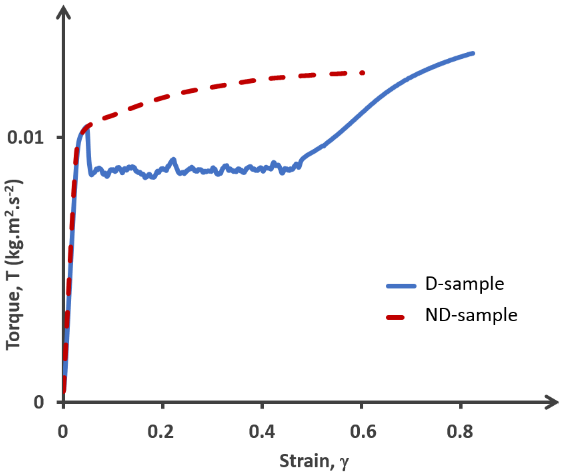

***Figure 4**: Torque – strain (γ at the surface of the sample) curves in torsion of the two cold-drawn ND- and D-samples.*

3.2.2. Wire surface

After cold-drawing, parallel longitudinal grooves are visible at the wire surface (Figure 5.a). Their frequency and intensity depend on the drawing conditions as line speed or cross-section reduction [32,34]. Though their origin is still under debate, they offer a helpful marker to quantify the amount of torsion and its homogeneity along the sample length. After 0.1 torsion strain, they are more pronounced than after cold-drawing, torsion increasing the intensity of the wire's surface roughness (Figure 5).

Even in the ND-sample, which does not delaminate during torsion, several cracks are observed beneath the wire surface (Figure 6). They systematically originate from a steel groove at the wire surface, filled with brass used for coating. Though the pearlitic microstructure is lightly revealed at high magnification (Figure 6.a), their relationship with the grain curling at the wire surface (Figure 3) is not straight. In this sample, the crack growth is stable: Its average length slightly grows up from 5 µm at a strain of 0.1 to 20 µm at a torsion strain of 0.3 (Figure 6.b). These cracks do not lead to rupture, the fracture surface after torsion being flat within the wire cross-section.

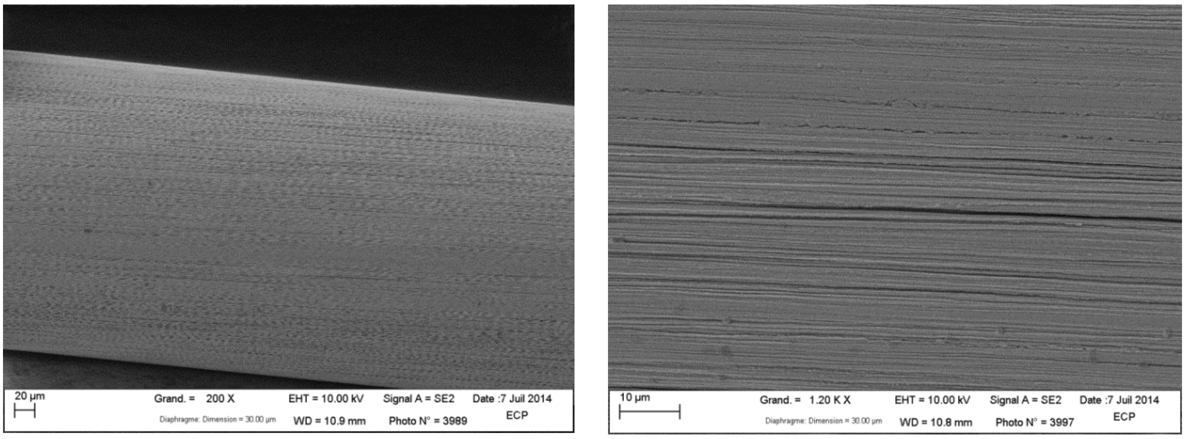

(a) (b)

***Figure 5**: Wire surface of ND-sample after a torsion strain equal to 0.1: general view of the wire (a); enlarged view (b). Longitudinal grooves are clearly visible on the enlarged view.*

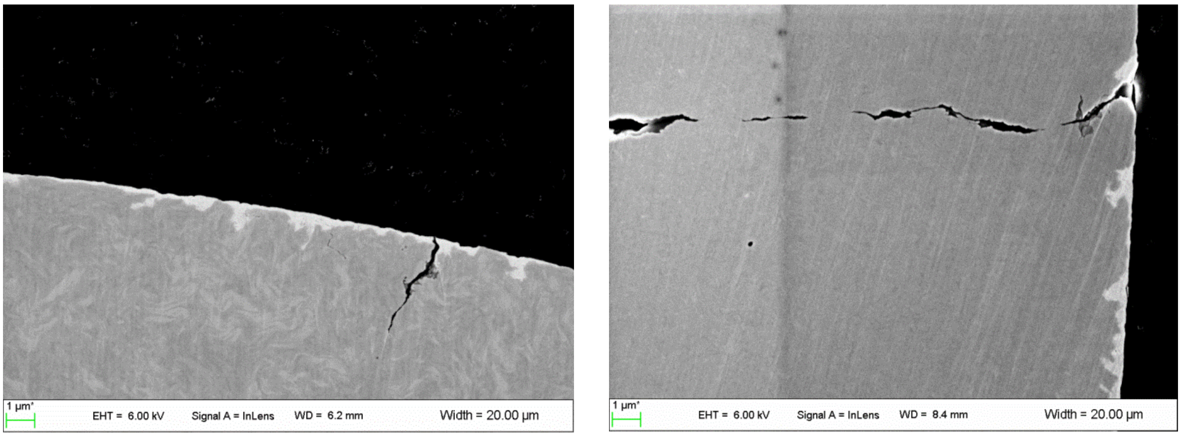

(a) (b)

***Figure 6**: Stable cracks beneath the wire surface (ND-sample), view in the cross-section: after a torsion strain of 0.1 (a), and 0.3 (b).*
The light grey layer and spots at the wire surface are residual traces of brass coating after cold drawing.

3.2.3. Subsurface microstructure

After torsion, the subsurface microstructure is observed by TEM. Thin foils are machined by FIB in the wire cross-section. ND-sample is twisted to 0.2, whereas D-sample is twisted to 0.06. These strain levels are the macroscopic ones, without considering local phenomenon ahead grooves or cracks.

In ND-sample twisted up to an applied strain of 0.2, the ribbon curled structure, inherited from drawing, is still visible with a main <110> component (Figure 7.a). Within most of the <110> grains, the orientation is less homogeneous than after drawing. This is mainly visible for the hoop direction (Figure 7.b). During torsion, new boundaries develop with an angle larger than 15°. They delineate fine grains that align along a wire radius below the groove (Figure 7.a). These fine grains, slightly elongated and curled, have a length between 200 and 500 nm. Their width is almost the same as after drawing.

In D-sample, twisted up to an applied strain of 0.06 in torsion, a thin foil was cut normally to a groove, close to an unstable crack and ahead of a shear band (Figure 8.a). The microstructure is much more irregular than the previous one in the ND-sample. Along a thin strip, in the radial direction under the groove (noted ‘S’ in Figure 8.b), the grains are slightly elongated parallel to the band direction and have a size between 50 and 100 nm for the shorter length and from 100 to 200 nm for the longer. Grains can be shared in two sets: a first, lying in a thin slice, along the wire radius below the grove (Figure 9.b); a second (Figure 9.a), composed by the curled <110> grains (mostly in green in Figure 8.b) on each part of the slice. {001} and {011} pole figures are calculated from the longitudinal IPF in each case. In the external domain (Figure 9.a), the grain orientation gives a <110> texture. Since the thin foil was cut on a plane normal to the groove direction, inclined by about 30° from the wire axis, it means these grains rotated as a whole during torsion. Within the shear band, evidence of <110> grains rotated by approximately 45° can be noticed, and the main grain orientation tends toward a simple shear texture (Figure 9.b).

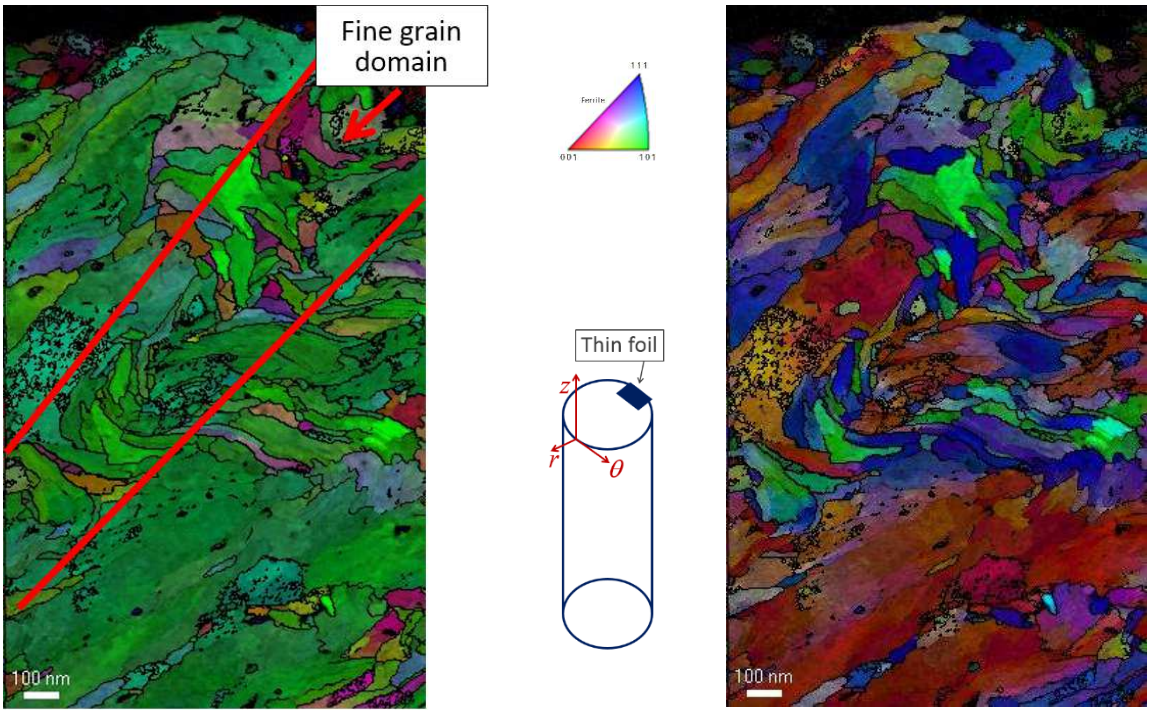

(a) (b)

Figure 7: *ASTAR orientation maps in the cross-section at the wire surface of ND-sample (γ= 0.2). IPF in the longitudinal (a) and hoop (b) directions (GB = 15°; IPF is superimposed with image quality).*

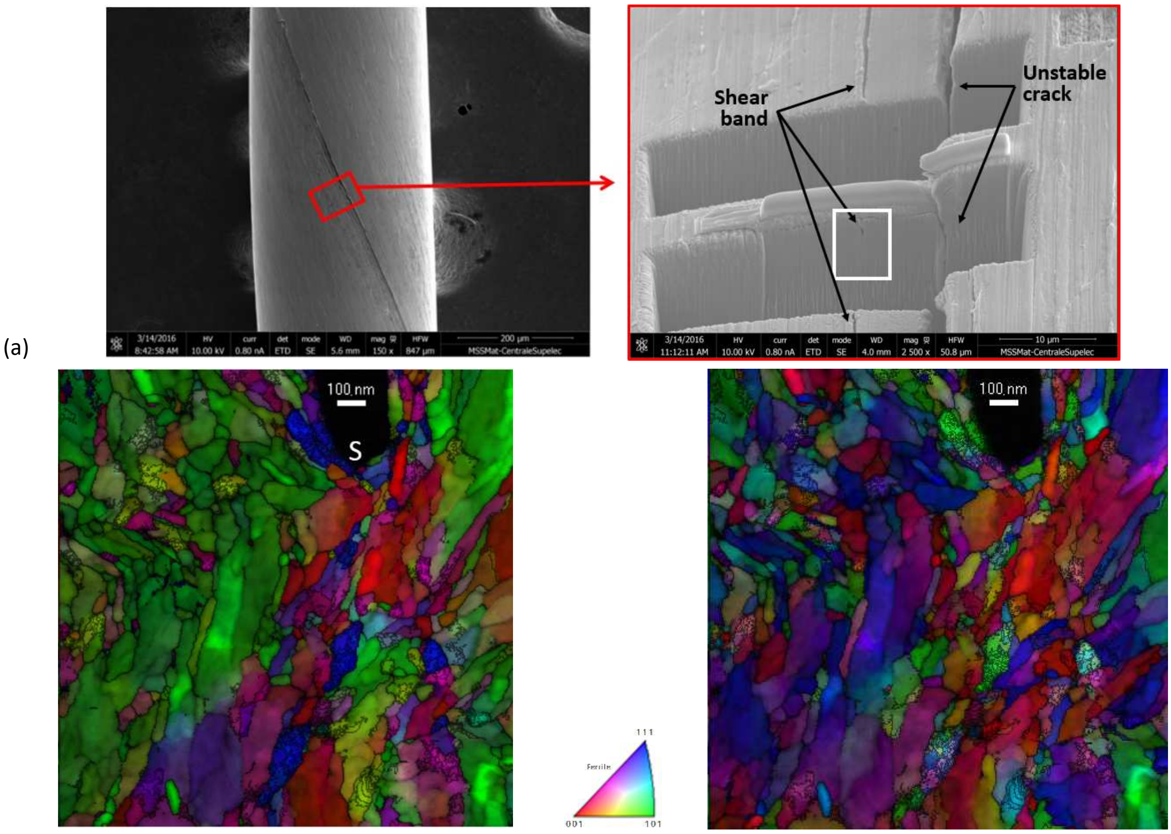

(b) (c)

Figure 8: *(a) SEM image of an unstable crack along D-sample after a torsion strain of 0.06 and a view of the thin foil machined by FIB (white rectangle) in a cross-section area containing a localized shear band, close to the unstable crack.*
ASTAR orientation maps of the thin foil in the longitudinal (b) and hoop (c) directions (GB = 15°; IPF is superimposed with image quality).

3.2.4. Stable and delamination cracks

To further understand crack initiation and growth during torsion, cross-section observations are performed in the cross-section of ND-sample after a torsion strain of 0.2, along a stable crack (Figure 10.e). Cracks are decorated by nanograins with a diameter between 10 and 30 nm (Figures 10.c and d). They define a narrow band, elongated along the cracks, crossing through the curled microstructure inherited from cold-drawing (Figures 10.a and b). Pole figures calculated from the grain orientation outside the shear band show a <110> texture rotated by 11° about the wire axis[1] (Figure 11.a). No definite grain orientation can be noticed in the shear band (Figure 11.b). Even restricted to the nanograins (grain size below 30 nm – GB = 15°), no specific texture clearly appears (Figure 11.c).

---

[1] Note in this case, the thin foil is normal to the wire axis and not to the groove direction.

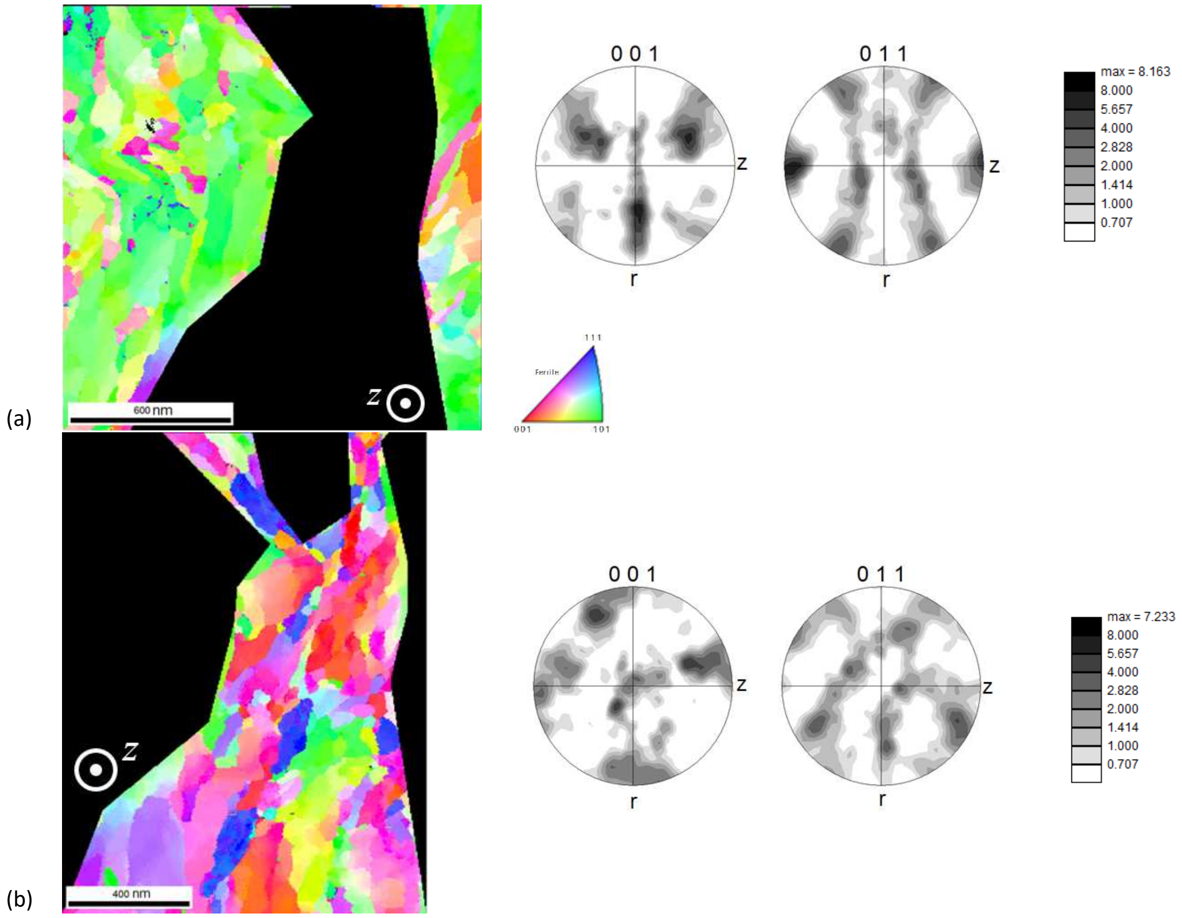

***Figure 9**: IPF in the radial direction of the microstructure under a longitudinal groove in D-sample (same as Figure 8).*
(a) Orientation map of the grains outside of the shear band and associated pole figures;
(b) Orientation map of the grains within the localized shear band and corresponding pole figures.

Additional observations were made on a delamination surface to check any difference with the microstructure along a stable crack. D-sample was twisted to the torque drop (Figure 4), which corresponds to the unstable propagation of a longitudinal crack through the wire cross-section, at least until the mid-diameter. A reverse torsion was then applied until the complete fracture, which occurs right at the plasticity onset. The fracture surface is shown in Figure 12.a. The right side of the micrograph corresponds to the delamination surface, parallel to the longitudinal section of the wire, extending from the wire surface almost to the wire center. The left part is the torn surface after the rupture in reverse torsion: The fracture surface clearly aligns with the elongated microstructure coming from the drawing (left side in Figure 12.a).

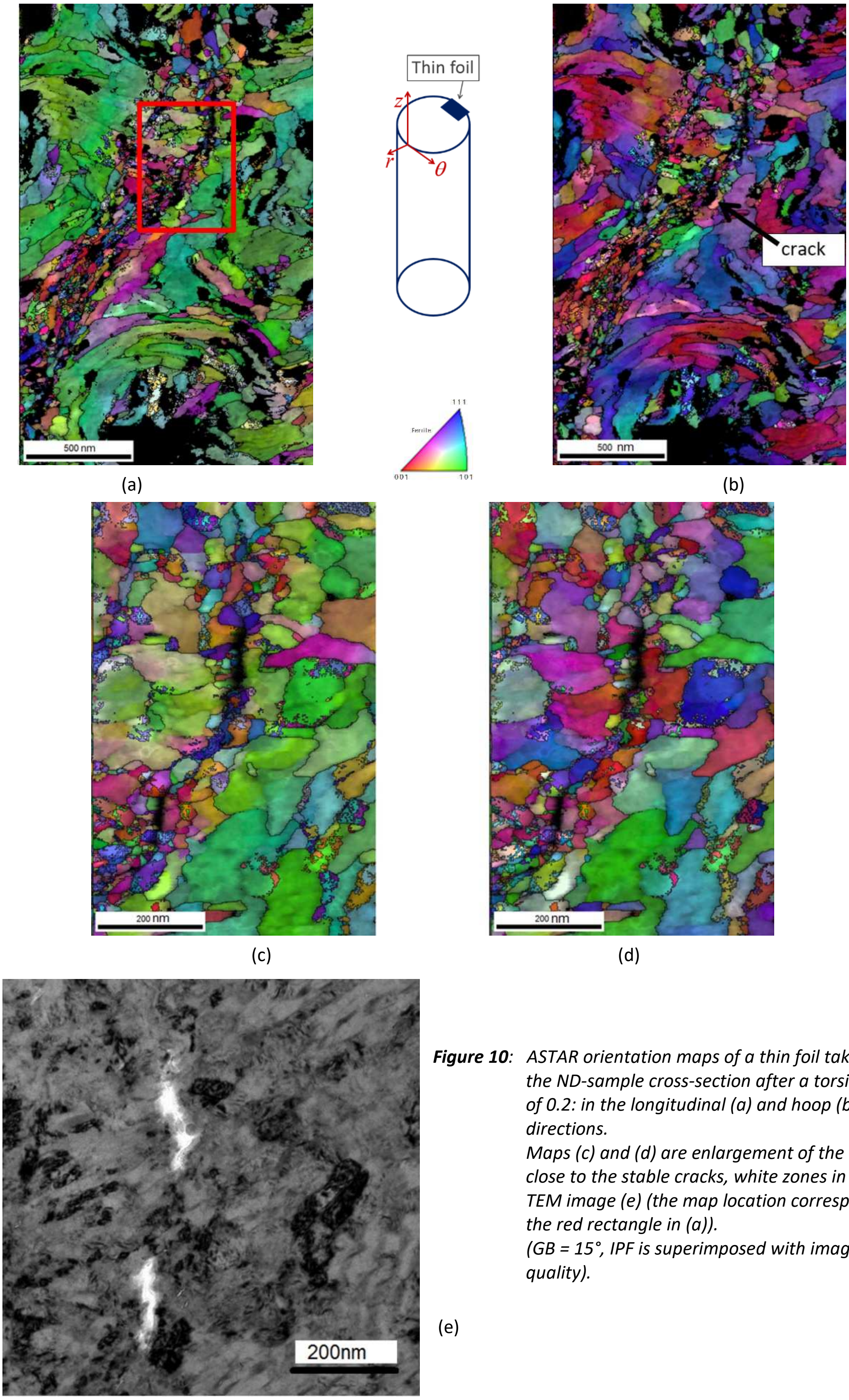

***Figure 10**: ASTAR orientation maps of a thin foil taken in the ND-sample cross-section after a torsion stain of 0.2: in the longitudinal (a) and hoop (b) directions.*
Maps (c) and (d) are enlargement of the area close to the stable cracks, white zones in the TEM image (e) (the map location corresponds to the red rectangle in (a)).
(GB = 15°, IPF is superimposed with image quality).

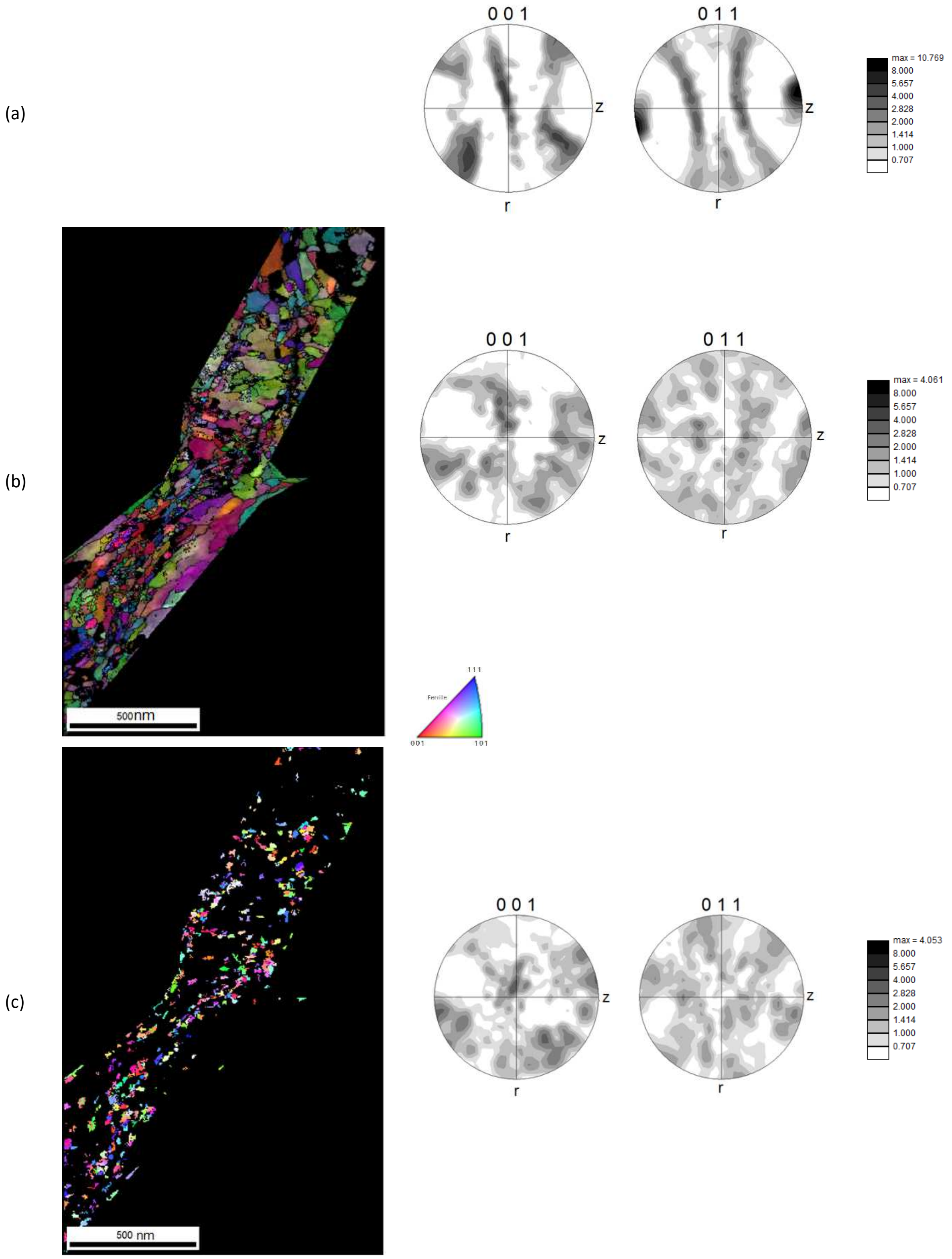

***Figure 11**: (a) Pole figures calculated from the orientations maps in Figure 10.a without the shear band containing the nanograins; (b) Orientation map of the shear band in the microstructure presented in Figure 10.a, and associated pole figures; (c) Orientation map of the nanograins within the shear band and corresponding pole figures (ND-sample; $\gamma = 0.2$).*

Delamination mechanism

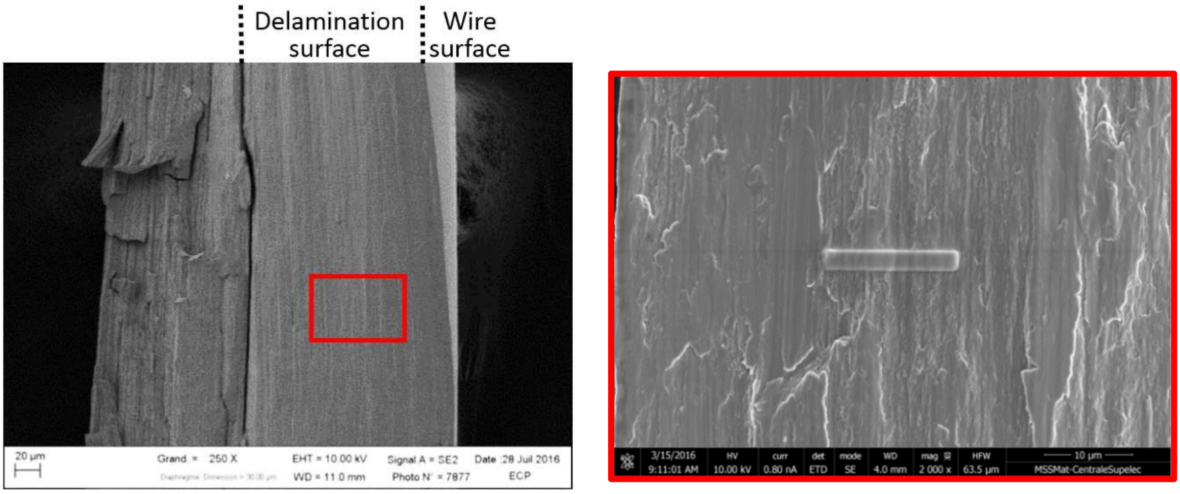

(a) (b)

***Figure 12**: SEM images of a delaminated wire (a), and of an enlarged zone (b); the rectangle in the middle of the image is the Pt coating, which protects the delamination surface during the FIB machining.*

At higher magnification, the delamination surface appears almost flat and somewhat regular (Figure 12.b). A thin rectangular platinum coating was deposited to protect the thin foil during FIB machining. Figures 13.a and b show the microstructure and the grain orientation in a subsurface area below the delamination surface in the transverse direction. A thin layer of nanograins whose size is evaluated between 10 and 30 nm decorates the fracture surface (Figure 13.b). A few tens of nanometers below, the curled grain microstructure is still clearly visible with a main <110> texture (Figures 13.a and b). However, it is also clear that the orientations of the nanograins are diverse. These different findings confirm former observations [50] and make visible a presumed microstructure that was unresolved by EBSD.

It can then be concluded that the microstructure along a delamination crack in D-sample (Figure 13.a) is very similar to the microstructure along stable cracks in ND-sample (Figure 10):

- a thin layer of nanograins decorating the crack surface;
- the same size of nanograins;
- large disorientation between nanograins compared to the main texture;
- and, outside of the nanograin domain, a persistence of the curled microstructure inherited to the cold drawing.

These are strong indications that the same mechanism occurs for stable and delamination cracks. This also prove that the nanograin bands exist before the appearance of cracks.

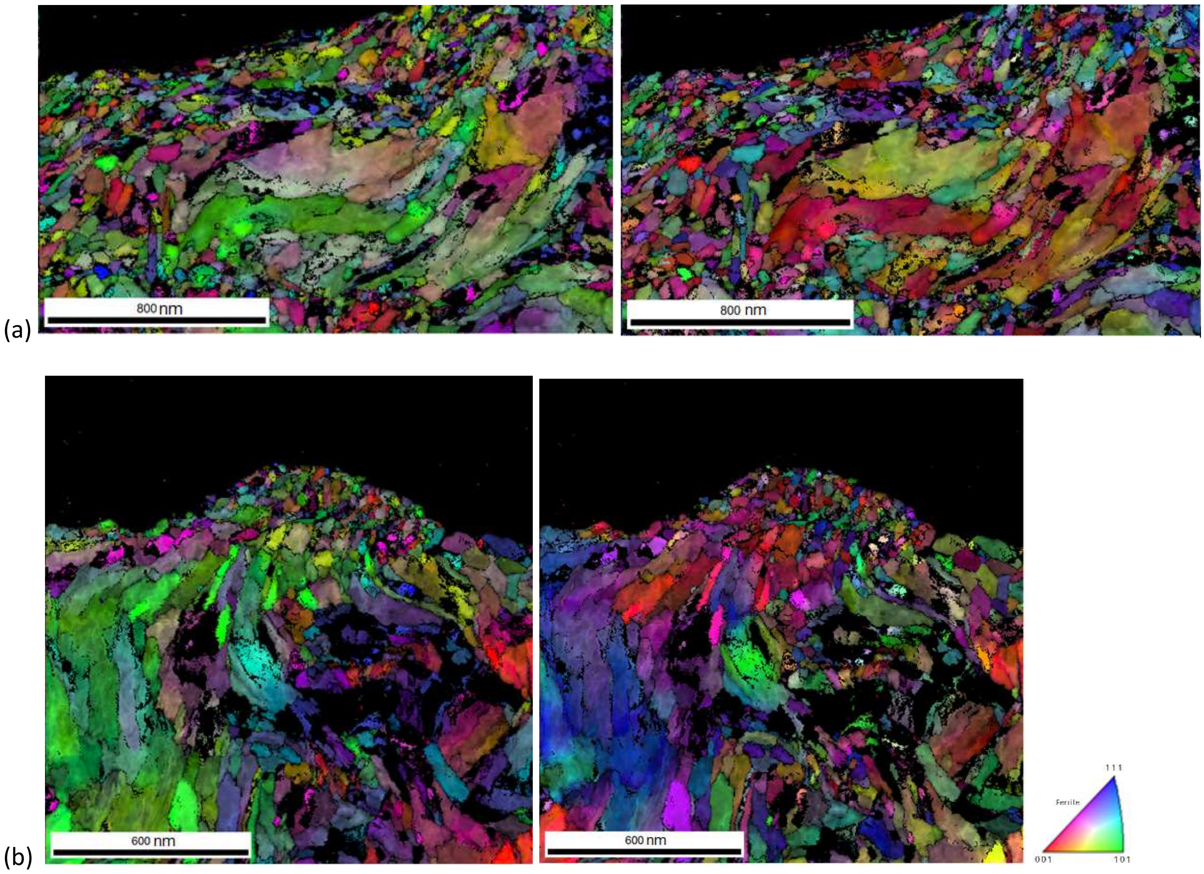

***Figure 13**: (a) ASTAR orientation maps in a normal section to the delamination surface (GB=15°, IPF in the longitudinal and hoop directions superimposed with image quality). (b) Detail at a higher magnification showing clearly the thin layer of nanograins.*
Note the location of the thin foil in Figure 12.b.

4. Discussion

4.1. Deformation mechanisms

4.1.1. Cold-drawing

The origin of grain curling during cold-drawing of pearlitic wire is well documented in the literature since the seminal work by [10,11,23,24]. It results from an intense <110> texture, which favors four equivalent slip systems during drawing. The fifth one, needed to accommodate the imposed strain tensor, required high deformation energy, as evidenced by a large value of the Taylor factor for the <110> grains [23]. Figure 14 clearly highlights this point: A Taylor simulation is done for the crystallographic orientations of the grains observed in Figure 2, assuming that the strain tensor imposed in each grain is strictly equal to the macroscopic drawing strain tensor (Figure 14.a). The curled grains ((*e.g.*, grain 'S' in Figure 14.a) have a Taylor factor equal to or higher than 4.3. The only grain with the lowest Taylor factor (grain ‘A’ in blue in Figure 14.a) has, in fact, a different orientation. From Figure 2.b, it appears to be close to <100>//z and <012>//r orientation. The almost rectangular shape of grain ‘A’ indicates that deformation is mostly imposed by the surrounding grains.

Plane strain conditions are fulfilled when only two slip systems among the four equivalent ones are active within the <110> grains. Two different Taylor simulations can thus be performed for two plane strain tensors rotated by π/2 in the wire cross-section. Figures 14.b and c compare the Taylor factor for the two simulations and show that the <110> grains divide into 'soft' and 'hard' orientations (*resp*. blue and red colors). The accommodation of the imposed strain is then completed by a rigid body rotation, which requires much less energy than five slip systems simultaneously active.

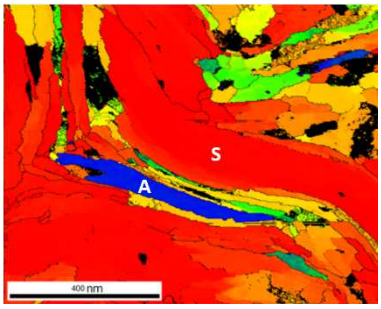

(a)

Figure 14: *Taylor factors calculated from the orientation map of Figure 2 (A and S refer to the same grains as in Figure 2).*
(a) corresponds to the drawing deformations (tension along the wire axis and compression in the radial directions),
(b) and (c) correspond to two different plane strain conditions.
The Taylor factor ranks between 2 ('soft' grains – in blue) to 4.3 ('hard' grains – in red).

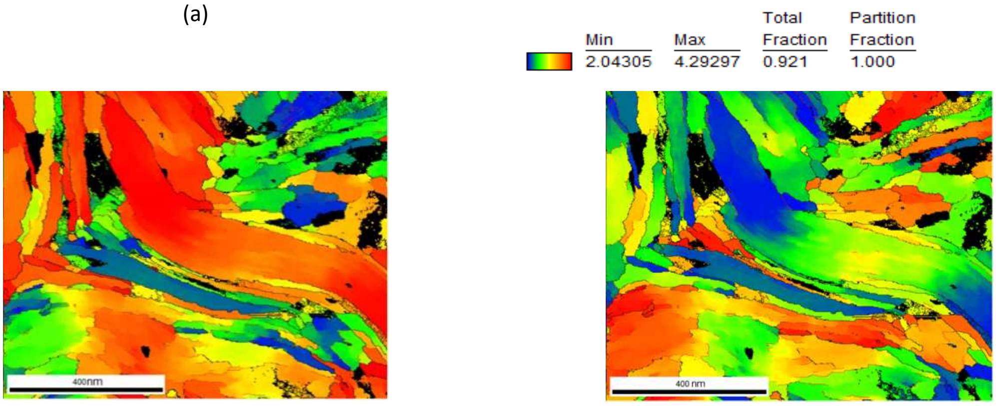

(b) (c)

Grains are less constrained at the wire surface. Therefore, they have more freedom to bend, creating bumps and grooves, as seen in Figure 3. Since grains are elongated after several drawing passes, this creates long groves along the wire surface. Subsequent passes generated a hoop compression on the groove edges, which leads to a localized kink within some <110> grains (Figure 3.b). This mechanism probably results in the fragmentation of the cementite lamellae within the kink band and in the formation of tilt sub-boundaries, as observed in the area 'A' in Figure 3.a).

4.1.2. Torsion behavior of cold-drawn wires

Equations (1) and (2) allow for computing the shear stress – shear strain curve at the wire surface from the torque – strain data. This yields more accurate information about the mechanical behavior of drawn wires under torsion (Figure 15). Oscillations at large strain mostly result from the torque derivation in Eq. (2). Though the ND sample does not delaminate during torsion, a stress peak is observed right after the yield stress (Figure 15). It comes from the change of strain path from drawing to torsion [32,42]. Since drawing imposed a strong microstructural anisotropy of the ferrite (texture and dislocation microstructure) and the alignment of cementite lamellae along the wire axis, the cross-effect resulting from the strain path change is maximum [38,59].

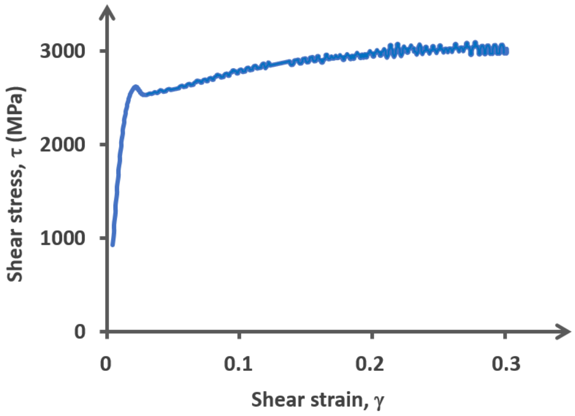

Figure 15*: Shear stress – shear strain curve in torsion for ND-sample.*

Due to the longitudinal anisotropy of the drawn wire at the onset of plasticity, shearing along the wire axis is much easier than shearing in the cross-section. The torsion is then accommodated by simple shear and a rigid body rotation [18]. The microstructure observations show that this mechanism is strongly heterogeneous. The results in Figure 9 evidence this. The groove inclination corresponds roughly to a local shear strain of 0.56, whereas the applied strain is equal to 0.06 because of the localization of torsion in this zone of the wire length. The pole figures, inside and outside the band, clearly show that the internal slice is, in fact, a localized shear band. This rotation corresponds to a local shear of about 1. Thus, the surface groove delineated a localized shear band, in which the strain is more than five times the imposed macroscopic strain, while the accommodation is obtained by a rigid body rotation on each side. The wire deforms in torsion similar to a deck of cards [18,60].

The microstructure along a stable crack in the ND sample gives a second example (Figure 10). A shear band is highlighted, oriented along the wire radius (Figure 11.b). Even if the applied torsion strain is 0.2, the local strain within the shear band is much larger than in the previous case. The pole figures calculated from the grain orientations outside the shear band again confirm a rigid body rotation on each part of the band (Figure 11.a). This induces a large shearing within the band. Moreover, cracks are not related to any specific grain orientation (Figure 11.b and c), which contradicts the hypothesis of a cleavage fracture, sometimes assumed to account for delamination [15].

4.2. Shear band localization and crack propagation

The shear bands can result from geometrical or microstructural reasons. First, the grooves, formed at the wire surface by the curled grains, generate stress concentration. A second hypothesis is that peculiar features of the drawn microstructure locally soften the wire.

The first hypothesis is tested by erasing the grooves at the wire surface after drawing. The wire surface is electro-polished in a perchloric acid solution for 20 s at 10 V. The polishing removes a layer of 5 and 10 µm smoothing the roughness inherited from cold-drawing (Figure 16.a). Torsion up to a strain of 0.3 reveals longitudinal grooves on the wire surface (Figure 16.b). Cross-section observations show that they are, in fact, associated with radial cracks with a depth up to 6 µm. The depth of these grooves shows that stress concentration, coming from drawing, is not the main reason for the localization of the deformation during torsion. The second hypothesis – an unfavorable microstructure inherited from the drawing – is thus to be investigated.

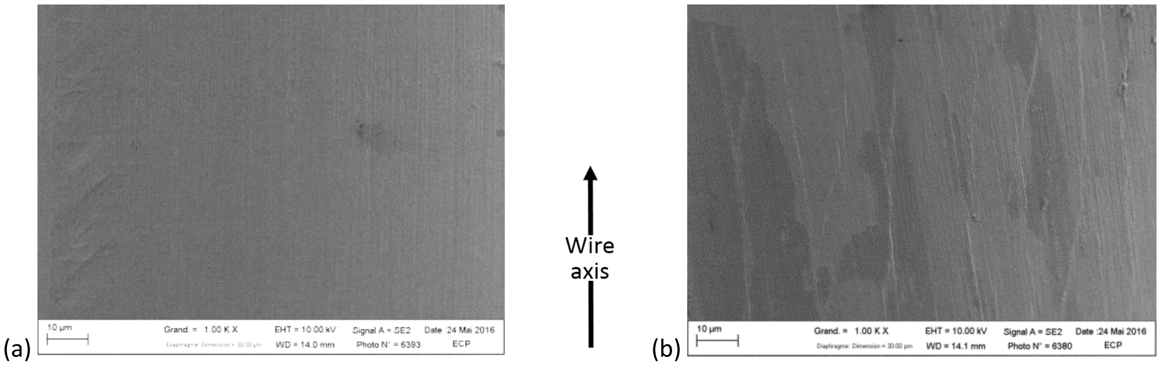

Figure 16: Wire surface after polishing (a), and after polishing and a torsion strain of 0.3 (b).

As shown above, macroscopic torsion is mainly accommodated by simple shear along the longitudinal direction. It means an easy path for dislocations exists along the wire axis for strain localization. This is achieved by the microstructural alignment along the wire axis. A second softening mechanism is needed to extend the shear band along the radial direction. Such a propagation seems difficult as the cementite lamellae are mostly parallel to the wire length and could act as strong obstacles to dislocations within the ferrite. However, beneath the most acute grooves, grains are strongly bent (area 'A' in Figure 3.a, for instance), which leads to the breakage of the cementite lamellae and even to a partial dissolution of cementite due to the high local strain [58]. This delineated an easy path for simple shear.

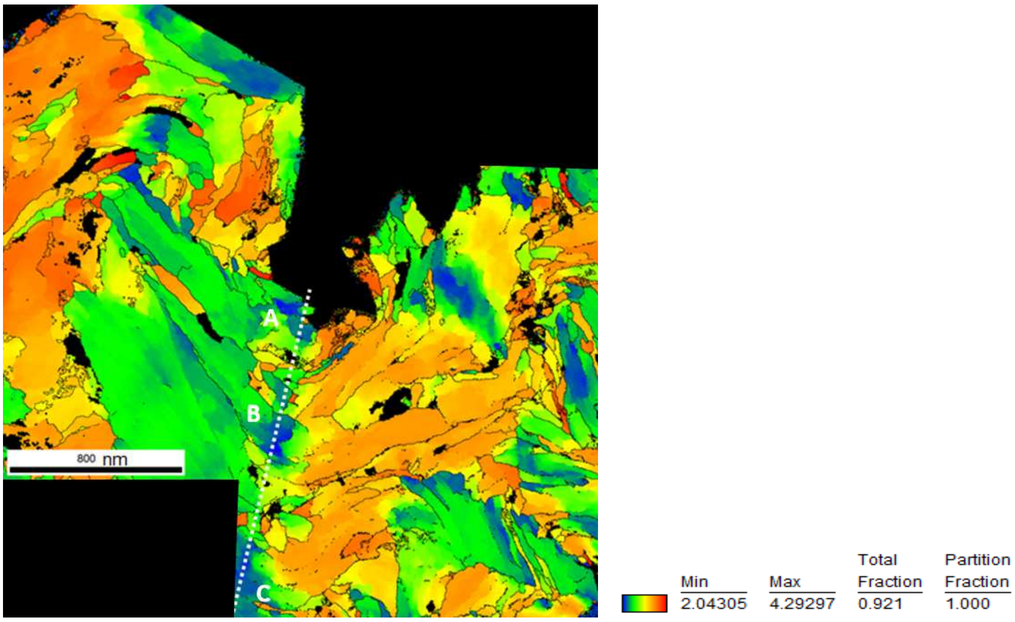

***Figure 17**: Taylor factors calculated for a simple shear on a radial plane (whose trace in the cross-section is the white dotted line) and in the longitudinal direction. The grain orientations are given in Figure 3. The Taylor factor is between 2 (in blue) to 4.3 (in red).*

An additional cause for strain localization comes from grain orientation after drawing. The <110> texture is such that, for an important localized bending, a {112} slip plane is aligned with the radial shear plan induced by torsion. Taylor simulations are performed on the microstructure presented in Figure 3 for a simple shear on a radial plane and parallel to the wire axis. Several grains have a very low Taylor factor (blue grains A, B, and C in Figure 17), which means simple shear is easy. Moreover, these grains are aligned along the wire radius (dotted line in Figure 17), which favors shear propagation along this direction.

These different results evidence the preliminary steps of crack formation. Since localized shear bands accommodate imposed torsion, the strain and strain rate are very high within these bands. The average distance between two bands is measured to about 10 µm, and their average width is around 500 nm. It means that the strain and strain rate are roughly 20 times their macroscopic values. At the crack initiation, the strain and strain rate in a band can thus be as high as 10 and 1 s^{-1}, respectively. This undoubtedly results in adiabatic heating; the temperature increase is estimated as:

$$\Delta T = \frac{\beta}{\rho.C_p}\int \tau d\gamma \qquad (3)$$

where τ is the shear stress, ρ the density, C_p the specific heat, and β a parameter which represents the fraction of deformation work dissipated in heat (usually taken as 0.9). For a shear stress of 2500 MPa for cold-drawn pearlitic steel and a shear strain of 0.5, the increase of temperature is of the order of 300°C if the diffusion is neglected, a weak assumption owing to the high strain rate. This local heating, combined with the large strain, is enough for continuous dynamic recrystallization.

The following observations confirm continuous dynamic recrystallization. When the deformation starts to localize close to the surface, a large strain is experienced within the grains in the band. Some grain fragmentations are visible with the appearance of subgrain boundaries. A few of them evolve toward grain boundaries, and several fine grains (100 to 200 nm) can be identified (Figure 7). The dynamic recrystallization is in its first step, as proved by the pole figure within the band where traces of rotated <110> grains are still evidenced (Figure 9.b). As the torsion test is continued, the strain increases in the shear band, and the continuous dynamic recrystallization progresses. One may assume that it is almost finished when a crack appears. The shear band is then mainly formed by nanograins (10 to 30 nm). The pole figures, restricted to the nanograins (grain size below 30 nm – GB = 15°), do not show any specific texture. This is a good indication that nanograins result from dynamic recrystallization in the localized shear band, as this was reported in iron after surface mechanical attrition [61] or in rail steel after fatigue [62,63], for instance. As the crack propagates toward the wire center, mode II propagation induces an intense shear in front of the crack tip, which allows the shear localization and the dynamic recrystallization to progress. So, the delamination crack is wholly decorated with nanograins when it reaches the center (Figure 13).

The last question concerns the propagation mechanism of the crack within the nanograin band. As there is no preferential orientation of the nanograins, it is almost impossible to assume cleavage fracture. After delamination, the fracture surface reveals a series of micro-holes so that a ductile fracture can be inferred (Figure 18.a). Moreover, a cross-section of a delaminated wire shows irregularities along the crack path (Figure 18.b). The typical size of these steps compares with the nanograins' mean size, which can be coherent with an intergranular propagation. Such a mechanism was already suggested by [41] and more recently by [64]. Even if cementite is largely dissolved locally, the interface between ferrite and carbon-rich phase, associated with former cementite lamella, is considered as a weak link [65]. It can then be concluded that delamination corresponds to a shear failure associated with shear bands [66].

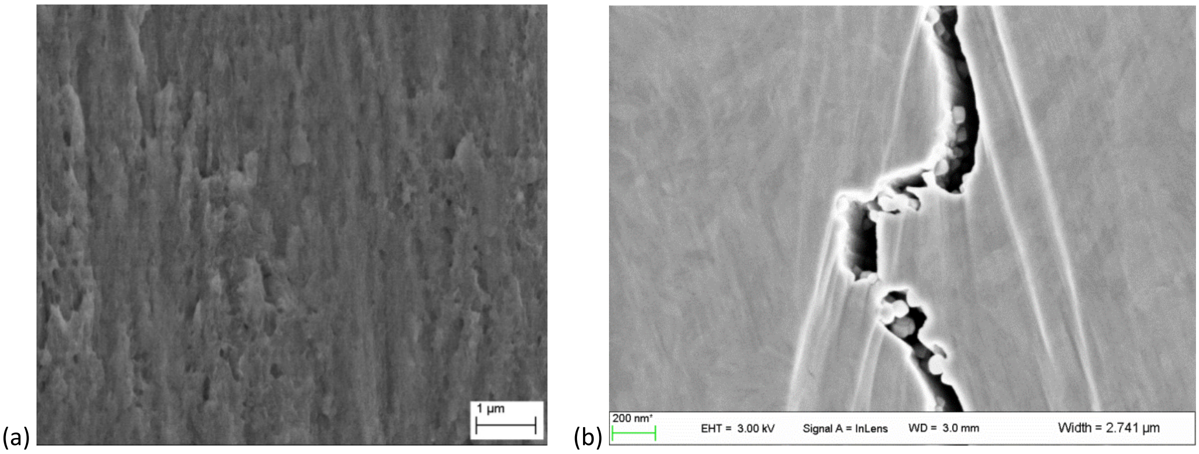

***Figure 18**: Magnification of the fracture surface (a) and SEM observation of a cross-section containing a crack (b).*

5. Conclusion

The microstructure of heavy cold-drawn pearlitic steel wires was characterized before and after torsion deformation. Significant results are highlighted:

- Below the grooves at the wire surface, grain orientations favor simple shear along the wire axis on a radial plane;
- During torsion, bands of nanograins are observed along the radial direction;
- On each side of these bands, crystallographic texture indicated a rigid body rotation, accommodating the local shear deformation within the bands.

These results allow to define different propagation steps and to draw a chronology of the initiation and propagation of delamination cracks:

(i) Shear localization under the most acute longitudinal grooves induces nanograin formation by continuous dynamic recrystallization;
(ii) The high local strain within the nanograin bands, 10 to 20 times the applied strain, leads to crack initiation;
(iii) Cracks mainly propagate by intergranular fracture along the nanograin boundaries.

Acknowledgments

The authors would like to sincerely thank Professor J.D. Embury for fruitful discussions throughout the project.

Data availability

The raw/processed data required to reproduce these findings cannot be shared at this time due to legal or ethical reasons.

References

[1] J.D. Embury, R.M. Fisher, The structure and properties of drawn pearlite, Acta Metall. 14 (1966) 147–159.
https://doi.org/10.1016/0001-6160(66)90296-3

[2] D. Raabe, P.P. Choi, Y. Li, A. Kostka, X. Sauvage, F. Lecouturier, K. Hono, R. Kirchheim, R. Pippan, D. Embury, Metallic composites processed via extreme deformation: Toward the limits of strength in bulk materials, MRS Bull. 35 (2010) 982–991.
https://doi.org/10.1557/mrs2010.703

[3] Y.J. Li, P. Choi, S. Goto, C. Borchers, D. Raabe, R. Kirchheim, Evolution of strength and microstructure during annealing of heavily cold-drawn 6.3 GPa hypereutectoid pearlitic steel wire, Acta Mater. 60 (2012) 4005–4016.
https://doi.org/10.1016/j.actamat.2012.03.006

[4] Y. Li, D. Raabe, M. Herbig, P.P. Choi, S. Goto, A. Kostka, H. Yarita, C. Borchers, R. Kirchheim, 2014. Segregation stabilizes nanocrystalline bulk steel with near theoretical strength. Phys. Rev. Lett. 113, 106104.
https://doi.org/10.1103/PhysRevLett.113.106104

[5] T. Takahashi, M. Nagumo, Y. Asano, Microstructures dominating ductility of eutectoid pearlitic steels, J. Jpn. Inst. Met. 42 (1978) 708–715.
https://doi.org/ 10.2320/jinstmet1952.42.7_708

[6] F.B. Pickering, B. Garbarz, The effect of transformation temperature and prior austenite grain size on the pearlite colony size in vanadium treated pearlitic steels, Scripta Metall. 21 (1987) 249–253.
https://doi.org/10.1016/0036-9748(87)90207-9

[7] B.L. Bramfitt, A.R. Marder, A transmission-electron-microscopy study of the substructure of high-purity pearlite, Mater. Charact. 39 (1997) 199–207.
https://doi.org/10.1016/S1044-5803(97)00122-8

[8] A. Walentek, M. Seefeldt, B. Verlinden, E. Aernoudt, P. Van Houtte, Electron backscatter diffraction on pearlite structures in steel, J. Microsc. 224 (2006) 256–263.
https://doi.org/10.1111/j.1365-2818.2006.01702.x

[9] Z.D. Li, G. Miyamoto, Z.G. Yang, T. Furuhara, Nucleation of austenite from pearlitic structure in an Fe–0.6C–1Cr alloy, Scripta Mater. 60 (2009) 485–488.
https://doi.org/10.1016/j.scriptamat.2008.11.041

[10] G. Langford, A study of the deformation of patented steel wire, Metall. Trans. 1 (1970) 465–477.
https://doi.org/10.1007/BF02811557

[11] G. Langford, Deformation of pearlite, Metall. Trans. 8A (1977) 861–875.
https://doi.org/10.1007/BF02661567

[12] J. Toribio, E. Ovejero, Effect of cumulative cold drawing on the pearlite interlamellar spacing in eutectoid steel, Scripta Mater. 39 (1998) 323–328.
https://doi.org/10.1016/S1359-6462(98)00166-3

[13] X. Zhang, A. Godfrey, N. Hansen, X. Huang, W. Liu, Q. Liu, Evolution of cementite morphology in pearlitic steel wire during wet wire drawing, Mater. Charact. 61 (2010) 65–72.
https://doi.org/10.1016/j.matchar.2009.10.007

[14] X. Zhang, A. Godfrey, N. Hansen, X. Huang, Hierarchical structures in cold-drawn pearlitic steel wire, Acta Mater. 61 (2013) 4898–4909. https://doi.org/10.1016/j.actamat.2013.04.057

[15] Y. Liu, Q. Jiang, G. Wang, Y. Wang, A. Tidu, L. Zuo, Influence of microstructures and textures on the torsional behavior of pearlitic wires, J. Mater. Sci. Technol. 21 (2005) 357–360.

[16] F. Yang, C. Ma, J.Q. Jiang, H.P. Feng, S.Y. Zhaib, Effect of cumulative strain on texture characteristics during wire drawing of eutectoid steels, Scripta Mater. 59 (2008) 850–853. https://doi.org/10.1016/j.scriptamat.2008.06.048

[17] M. Zidani, S. Messaoudi, T. Baudin, D. Solas, M.H. Mathon, Deformation textures in wire drawn perlitic steel, Int. J. Mater. Form. 3 (2010) 7–11 https://doi.org/10.1007/s12289-009-0410-3

[18] Y. Liu, Y. Zhang, A. Tidu, L. Zuo, <110> Fiber texture evolution of ferrite wires during drawn-torsion and drawn-annealing-torsion process, J. Mater. Sci. Technol. 28 (2012) 1010–1014. https://doi.org/10.1016/S1005-0302(12)60166-2

[19] S. Gondo, R. Tanemura, R. Mitsui, S. Kajino, M. Asakawa, K. Takemoto, K. Tashima, S. Suzuki, Relationship between mesoscale structure and ductility of drawn high carbon steel wire, Mater. Sci. Eng. A 800 (2021) 140283. https://doi.org/10.1016/j.msea.2020.140283

[20] Y. Kanetsuki, R. Ogawa, Influence of texture on the torsional deformation behavior of drawn pearlitic carbon steel wires, in: S. Nagashima and N.T. Kyōkai (Eds.), Proc. of The Sixth Int. Conf. on Textures of Materials (ICOTOM 6), Iron and Steel Institute of Japan Pub., Tokyo(Japan), 1981, pp. 1127–1136.

[21] T. Montesin, J.J. Heizmann, Evolution of crystallographic texture in thin wires, J. Appl. Cryst. 25 (1992) 665–673. https://doi.org/10.1107/S0021889892004849

[22] M. Zelin, Microstructure evolution in pearlitic steels during wire drawing, Acta Mater. 50 (2002) 4431–4447. https://doi.org/10.1107/S0021889892004849

[23] W.F. Hosford, Microstructural changes during deformation of [011] fiber-textured metals, Trans. Met. Soc. AIME 230 (1964) 12–15.

[24] J. Gil Sevillano, L. Matey Muñoz, J. Flaquer Fuster, Ciels de Van Gogh et propriétés mécaniques, J. Phys. IV 8 (1998) PR4-155–165. (*in French*) https://doi.org/10.1051/jp4:1998419

[25] J. Languillaume, G. Kapelski, B. Baudelet, Cementite dissolution in heavily cold drawn pearlitic steel wires, Acta Mater. 45 (1997) 1201–1212. https://doi.org/10.1016/S1359-6454(96)00216-9

[26] A. Lamontagne, V. Massardier, X. Kléber, X. Sauvage, D. Mari, Comparative study and quantification of cementite decomposition in heavily drawn pearlitic steel wires, Mater. Sci. Eng. A 644 (2015) 105–113. https://doi.org/10.1016/j.msea.2015.07.048

[27] C. Borchers, R. Kirchheim, Cold-drawn pearlitic steel wires, Prog. Mater. Sci. 82 (2016) 405–444.

https://doi.org/10.1016/j.pmatsci.2016.06.001

[28] N. Guelton, M. François, Strain-induced dissolution of cementite in cold-drawn pearlitic steel wires, Metall. Mater. Trans. 51A (2020) 1602–1613. https://doi.org/10.1007/s11661-020-05640-4

[29] W.J. Nam, C.M. Bae, Void initiation and microstructural changes during wire drawing of pearlitic steels, Mater. Sci. Eng. A 203 (1995) 278–285. https://doi.org/10.1016/0921-5093(95)09826-7

[30] M. Herbig, D. Raabe, Y.J. Li, P. Choi, S. Zaefferer, S. Goto, 2014. Atomic-scale quantification of grain boundary segregation in nanocrystalline material. PRL. 112, 126103. https://doi.org/10.1103/PhysRevLett.112.126103

[31] Y.J. Li, A. Kostka, P. Choi, S. Goto, D. Ponge, R. Kirchheim, D. Raabe, Mechanisms of subgrain coarsening and its effect on the mechanical properties of carbon-supersaturated nanocrystalline hypereutectoid steel, Acta Mater. 84 (2015) 110–123. https://doi.org/10.1016/j.actamat.2014.10.027

[32] I. Lefever, U. D'Haene, W. Van Raemdonck, E. Aernoudt, P. Van Houtte, J. Gil Sevillano, Modeling of the delamination of high strength steel wire, Wire Journal International (Nov. 1998) 90–95.

[33] T. Shinohara, K. Yoshida, Deformation analysis of surface flaws in stainless steel wire drawing, J. Mater. Proc. Technol. 162-163 (2005) 579–584. https://doi.org/10.1016/j.jmatprotec.2005.02.125

[34] S.-K. Lee, S.-B. Lee, B.-M. Kim, Process design of multi-stage wet wire drawing for improving the drawing speed for 0.72 wt% C steel wire, J. Mater. Proc. Technol. 210 (2010) 776-783. https://doi.org/10.1016/j.jmatprotec.2010.01.007

[35] A. Phelippeau, S. Pommier, T. Tsakalakos, M. Clavel, C. Prioul, Cold drawn steel wires—processing, residual stresses and ductility—part I: metallography and finite element analyses, Fatigue Fract. Eng. Mater. Struct. 29 (2006) 243–253. https://doi.org/10.1111/j.1460-2695.2005.00981.x

[36] J. Toribio, F.J. Ayaso, B. González, J.C. Matos, D. Vergara, M. Lorenzo, 2016. Tensile fracture behavior of progressively-drawn pearlitic steels. Metals. 6, 114. https://doi.org/10.3390/met6050114

[37] A. Durgaprasad, S. Giri, S. Lenka, S. Kundu, S. Mishra, S. Chandra, R.D. Doherty, I. Samajdar, Microstructures and mechanical properties of as-drawn and laboratory annealed pearlitic steel wires, Metall. Mater. Trans. 48A (2017) 4583–4597. https://doi.org/10.1007/s11661-017-4269-5

[38] T.Z. Zhao, H.W. Song, S.H. Zhang, Non-monotonic radial distribution of tensile yielding in cold-drawn pearlitic wire, Mater. Sci. Technol. 34 (2018) 35–41. https://doi.org/10.1080/02670836.2017.1352642

[39] X. Zhang, A. Godfrey, X. Huang, N. Hansen, Q. Liu, Microstructure and strengthening mechanisms in cold-drawn pearlitic steel wire, Acta Mater. 59 (2011) 3422–3430. https://doi.org/10.1016/j.actamat.2011.02.017

[40] L. Zhou, F. Fang, L. Wang, H. Chen, Z. Xie, J. Jiang, Torsion delamination and recrystallized cementite of heavy drawing pearlitic wires after low temperature annealing, Mater. Sci. Eng. A 713 (2018) 52–60.

https://doi.org/10.1016/j.msea.2017.12.055

[41] F. Zok, J.D. Embury, On the analysis of delamination fractures in high-strength steels, Met. Trans. 21A (1990) 2565–2575. https://doi.org/10.1007/BF02647002

[42] W. Van Raemdonck, I. Lefever, U. D'Haene, Torsion tests as a tool for high strength wire evaluation, Wire Journal International (June 1994) 68–75.

[43] Y.S. Yang, J.G. Bae, C.G. Park, Nanostructure and mechanical properties of heavily cold-drawn steel wires, Mater. Sci. Eng. A 508 (2009) 148–155. https://doi.org/10.1016/j.msea.2008.12.036

[44] X. Hu, L. Wang, F. Fang, Z. Ma, Z. Xie, J. Jiang, Origin and mechanism of torsion fracture in cold-drawn pearlitic steel wires, J. Mater. Sci. 48 (2013) 5528–5535. https://doi.org/10.1007/s10853-013-7347-0

[45] S. Das, P. Koli, J. Mathur, A. D, T. Bhattacharyya, S. Bhattacharyya, Failure analysis of motor tire bead wires during torsion test, J. Fail. Anal. and Preven. 13 (2013) 684–688. https://doi.org/10.1007/s11668-013-9750-x

[46] L. Godecki, Phenomena associated with the torsional deformation of steel wires, Wire Industry (1971) 719–724.

[47] C.M. Bae, W.J. Nam, C.S. Lee, Effect of interlamellar spacing on the delamination of pearlitic steel wires, Scripta Mater. 35 (1996) 641–646. https://doi.org/10.1016/1359-6462(96)00183-2

[48] K. Shimizu, N. Kawabe, Fracture mechanics aspects of delamination occurrence in high-carbon steel wire, in: 2001 Conf. Proc. of The Wire Association International, Wire & Cable Technical Symposium (WCTS) 71st Annual Convention Atlanta, Georgia (USA), 2001, pp. 35–45.

[49] B. Goes, A. Martin-Meizoso, G. Gil Sevillano, Fragmentation of as-drawn pearlitic steel wires during torsion tests, Eng. Fracture Mech. 60 (1998) 255–262. https://doi.org/10.1016/S0013-7944(98)00023-X

[50] M. Tanaka, H. Saito, M. Yasumaru, K. Higashida, Nature of delamination cracks in pearlitic steels, Scripta Mater. (2016) 32–36. https://doi.org/10.1016/j.scriptamat.2015.09.004

[51] P.F. Willemse, B.P. Naughton, Effect of small drawing reductions on residual surface stresses in thin cold-drawn steel wire, as measured by X-Ray diffraction, Mater. Sci. Technol. 2 (1985) 41–44.

[52] J.A. Bailey, J.Y. Sheikh-Ahmad, Fundamental aspects of torsional loading, in: H. Kuhn and D. Medlin (Eds.), Mechanical Testing and Evaluation, ASM Handbook, vol.8, ASM International, 2000. https://doi.org/10.31399/asm.hb.v08.9781627081764

[53] S. Lozano-Perez, A guide on FIB preparation of samples containing stress corrosion crack tips for TEM and atom-probe analysis, Micron 39 (2008) 320-328. https://doi.org/10.1016/j.micron.2007.12.003

[54] E. Rauch, M. Veron, Coupled microstructural observations and local texture measurements with an automated crystallographic orientation mapping tool attached to a TEM, Mat.-wiss. u. Werkstofftech. 36 (2005) 552–556. https://doi.org/10.1002/mawe.200500923

[55] N. Guo, B.F. Luan, B.S. Wang, Q. Liu, Microstructure and texture evolution in fully pearlitic steel during wire drawing, Science China Technol. Sci. 56 (2013) 1139–1146. https://doi.org/10.1007/s11431-013-5184-7

[56] A. Jamoneau, J.H. Schmitt, D. Solas, 2017. Measurement of texture gradient in heavily cold-drawn pearlitic wires. Adv. Eng. Mater. 1700279. https://doi.org/ 10.1002/adem.201700279

[57] T.Z. Zhao, G.-L. Zhang, H.-W. Song, M. Cheng, S.H. Zhang, Crystallographic texture difference between center and sub-surface of thin cold-drawn pearlitic steel wires, J. Mater. Eng. Perf. 23 (2014) 3279–3284. https://doi.org/10.1007/s11665-014-1098-1

[58] F. Fang, L. Zhou, X. Hu, X. Zhou, Y. Tu, Z. Xie, J. Jiang, Microstructure and mechanical properties of cold-drawn pearlitic wires affect by inherited texture, Mater. and Design 79 (2015) 60–67. https://doi.org/10.1016/j.matdes.2015.04.036

[59] J.H. Schmitt, E.L. Shen, J.R. Raphanel, A parameter for measuring the magnitude of a change of strain path: validation and comparison with experiments on low carbon steel, Int. J. Plasticity 10 (1994) 535–551. https://doi.org/10.1016/0749-6419(94)90013-2

[60] Y.D. Liu, A. Tidu, B. Bolle, L. Zuo, J.J. Heizmann, Torsional modelisation of the torsion texture of steel cord, Mater. Sci. Forum, 408-4 (2002) 457–462.

[61] N.R. Tao, Z.B. Wang, W.P. Tong, M.L. Sui, J. Lu, K. Lu, An investigation of surface nanocrystallization mechanism in Fe induced by surface mechanical attrition treatment, Acta Mater. 50 (2002) 4603–4616. https://doi.org/10.1016/S1359-6454(02)00310-5

[62] R. Pan, R. Ren, C. Chen, X. Zhao, Formation of nanocrystalline structure in pearlitic steels by dry sliding wear, Mater. Charact. 132 (2017) 397–404. https://doi.org/10.1016/j.matchar.2017.05.031

[63] C.G. He, H.H. Ding, L.B. Shi, J. Guo, E. Meli, Q.Y. Liu, A. Rindi, Z.R. Zhou, W.J. Wang, 2020. On the microstructure evolution and nanocrystalline formation of pearlitic wheel material in a rolling-sliding contact. Mater. Charact. 164, 110333. https://doi.org/10.1016/j.matchar.2020.110333

[64] B.N. Jaya, S. Goto, G. Richter, C. Kirchlechner, G. Dehm, Fracture behavior of nanostructured heavily cold drawn pearlitic steel wires before and after annealing, Mater. Sci. Eng. A 707 (2017) 164–171. https://doi.org/10.1016/j.msea.2017.09.010

[65] T. Leitner, S.Sackl, B. Völker, H. Riedl, H. Clemens, R.Pippan, A. Hohenwarter, Crack path identification in a nanostructured pearlitic steel using atom probe tomography, Scripta Mater. 142 (2018) 66–69. https://doi.org/10.1016/j.scriptamat.2017.08.025

[66] A. Pineau, A.A. Benzerga, T. Pardoen, Failure of metals I: Brittle and ductile fracture, Acta Mater. 107 (2016) 424–483. https://doi.org/10.1016/j.actamat.2015.12.034